ELSEVIER

Contents lists available at ScienceDirect

#### European Journal of Cell Biology

journal homepage: www.elsevier.com/locate/ejcb





# The Kelch 3 motif on gigaxonin mediates the interaction with NUDCD3 and regulates vimentin filament morphology

Cassandra L. Phillips <sup>a</sup>, Christina So <sup>a</sup>, Meredith F. Gillis <sup>a</sup>, Jonathan Harrison <sup>a</sup>, Chih-Hsuan Hsu <sup>a</sup>, Diane Armao <sup>b,c</sup>, Natasha T. Snider <sup>a,\*</sup> <sup>o</sup>

- <sup>a</sup> Department of Cell Biology and Physiology, University of North Carolina at Chapel Hill, United States
- b Department of Pathology and Laboratory Medicine, University of North Carolina at Chapel Hill, United States
- <sup>c</sup> Department of Radiology, University of North Carolina at Chapel Hill, United States

#### ARTICLE INFO

# Keywords: Gigaxonin Kelch domain Intermediate filaments Cytoskeleton Chaperone NUDCD3 Neurodegenerative disease

#### ABSTRACT

Gigaxonin is an intermediate filament (IF)-interacting partner belonging to the Kelch-like (KLHL) protein family. Gigaxonin is encoded by the KLHL16 gene, which is mutated in Giant Axonal Neuropathy (GAN). The lack of functional gigaxonin in GAN patient cells impairs IF proteostasis by affecting IF protein degradation and transport. This leads to focal abnormal accumulations of IFs and compromised cellular function, with neurons being most severely impacted. We hypothesized that gigaxonin forms molecular interactions via specific sequence motifs to regulate IF proteostasis. The goal of this study was to examine how distinct Kelch motifs on gigaxonin regulate IF protein degradation and filament morphology. We analyzed vimentin IFs in HEK293 cells overexpressing wild type (WT) gigaxonin, or gigaxonin lacking each of the six individual Kelch motifs, K1-K6. All six gigaxonin deletion mutants ( $\Delta$ K1- $\Delta$ K6) promoted the degradation of soluble vimentin. Compared to WTgigaxonin, AK3-gigaxonin exhibited increased soluble vimentin degradation and increased presence of thick bundles of vimentin IFs. The  $\Delta$ K4 mutant showed similar, but milder phenotypes compared to  $\Delta$ K3. Using mass spectrometry proteomics we found that, relative to WT gigaxonin, AK3 gigaxonin had increased associations with ubiquitination-associated and mitochondrial proteins but lost the association with the NudC domaincontaining protein 3 (NUDCD3), a molecular chaperone enriched in the nervous system. AlphaFold modeling revealed loss of gigaxonin-NUDCD3 binding with ΔK3 and altered binding with ΔK4. Collectively, our cell biological data show the induction of an abnormal GAN-like IF phenotype in cells expressing ΔK3- and, to a lesser extent, AK4-gigaxonin, while our proteomic profiling links the loss of gigaxonin-NUDCD3 interactions with defective IF proteostasis.

#### 1. Introduction

Gigaxonin is an intermediate filament (IF)-interacting partner that belongs to the 42-member family of Kelch-like (KLHL) proteins (Bomont et al., 2000; Shi et al., 2019). KLHL proteins form diverse molecular interactions and regulate protein degradation and trafficking in different cell types (Dhanoa et al., 2013). Precise functioning of KLHLs is essential in the muscle and brain, which is evident by the physiological effects of disease-causing mutations within this gene family.

KLHL16 (or GAN) is the gene that encodes gigaxonin, and it is mutated in the neurodegenerative disease Giant Axonal Neuropathy (GAN) (Bharucha-Goebel et al., 2021). The lack of functional gigaxonin in GAN patient cells impairs IF proteostasis, leading to defective IF

dynamics, focal abnormal accumulation of IF proteins, and compromised cellular function, especially in neurons (Johnson-Kerner et al., 2014). Molecular-level understanding of gigaxonin-IF interactions can provide new insights into IF network regulation and GAN pathogenesis.

Gigaxonin interacts with IF protein substrates via its  $\sim$ 300 amino acid-spanning C-terminal Kelch domain (Johnson-Kerner et al., 2015). The Kelch domain is composed of six individual Kelch motifs (K1-K6), but the significance of this large domain and its individual motifs on IF proteostasis is not clear. We observed that many clinical variants impacting the Kelch domain of gigaxonin have high predicted pathogenicity based on protein structure models (Cheng et al., 2023). With the aim of advancing knowledge of the functional and disease relevance of gigaxonin, we sought to determine how the deletion of each individual

E-mail address: ntsnider@med.unc.edu (N.T. Snider).

<sup>\*</sup> Corresponding author.

Kelch motif on gigaxonin affects its function.

To accomplish this, we compared soluble vimentin protein levels and vimentin IF organization in HEK293 cells overexpressing wild type gigaxonin or gigaxonin lacking each of the six Kelch motifs. Unexpectedly, our data revealed a disconnect between the levels of soluble vimentin, which is the substrate for gigaxonin-induced degradation (Renganathan et al., 2023), and effects on filament morphology. We conducted mass spectrometry proteomics, which revealed new gigaxonin interactors, and uncovered a novel interaction between gigaxonin and the NUDCD3 chaperone. The findings point to a potential new mechanism behind the pathologic effect of gigaxonin deficiency and may help to explain high pathogenicity predictions from the structure-based analysis of gigaxonin variants affecting specific segments of the large Kelch domain.

#### 2. Results

## 2.1. Distribution of known and predicted pathogenic variants across the gigaxonin protein domains

Based on the genetic analysis from a GAN natural history study (Bharucha-Goebel et al., 2021), the majority of the pathogenic variants are gigaxonin missense mutations (Fig. 1A). The missense mutations are spread across the three gigaxonin domains (BTB, BACK, and Kelch) without any evidence for 'hotspots', and there is currently no known genotype-phenotype correlation (Bharucha-Goebel et al., 2021). The recently developed deep learning model AlphaMissense uses sequence-based structural protein models to assign pathogenicity scores for variants (Cheng et al., 2023). For missense variants reported in the natural history study of GAN patients (Bharucha-Goebel et al., 2021), this tool accurately predicted the high pathogenicity of 19/22 variants with median score of 0.9850, on a scale from 0 to 1 (Fig. 1B). Therefore, we applied AlphaMissense to all GAN coding missense variants classified as uncertain significance, likely pathogenic, or pathogenic in the NIH

ClinVar database (Landrum et al., 2018) (Fig. 1C). Many GAN variants had high pathogenicity scores (red dots) that were similar to those of the known disease-causing variants (black dots). Since  $\sim\!50\,\%$  of the gigaxonin sequence comprises the Kelch domain, it is not surprising that this domain had the most reported variants, with both benign and pathogenic prediction scores (Fig. 1D). Moreover, the gigaxonin Kelch domain interacts with IF protein substrates (Johnson-Kerner et al., 2015), but how each individual segment of this domain contributes to overall gigaxonin function is not known. Therefore, in this study we were specifically interested in investigating the roles of each individual Kelch motif on IF regulation.

## 2.2. Individual gigaxonin Kelch deletion mutants retain the ability to promote vimentin degradation

We utilized a full-length human gigaxonin construct incorporating a C-terminal turbo-GFP (tGFP) tag (Fig. 2A). We used soluble vimentin to measure gigaxonin activity because soluble vimentin accumulates robustly upon gigaxonin knockout, suggesting that it is the substrate for gigaxonin (Renganathan et al., 2023). Both GFP-tagged (GFP-Gig) and untagged gigaxonin reduced soluble vimentin levels when transfected in HEK293 cells, showing that the GFP tag did not interfere with the vimentin degradation-promoting function of gigaxonin (Fig. 2B-C). Using the validated GFP-tagged gigaxonin, we analyzed the impact of individual Kelch motif deletions on gigaxonin function. The six Kelch motifs on gigaxonin form a beta-propeller structure that facilitates binding interactions with IF proteins and potentially other gigaxonin substrates and regulators (Boizot et al., 2014) (Fig. 2D). We generated constructs of gigaxonin lacking each of the six Kelch motifs: ΔKelch 1 ( $\Delta$ K1: aa274–326).  $\Delta$ Kelch 2 ( $\Delta$ K2: aa327–374).  $\Delta$ Kelch 3 ( $\Delta$ K3: aa376–421), ΔKelch 4 (ΔK4; aa422–468), ΔKelch 5 (ΔK5; aa470–522), and  $\Delta$ Kelch 6 ( $\Delta$ K6; aa528–574). Immunoblot analysis showed the expression of gigaxonin consistent with the presence of each deletion (Fig. 2E). Notably, endogenous gigaxonin is expressed at very low levels

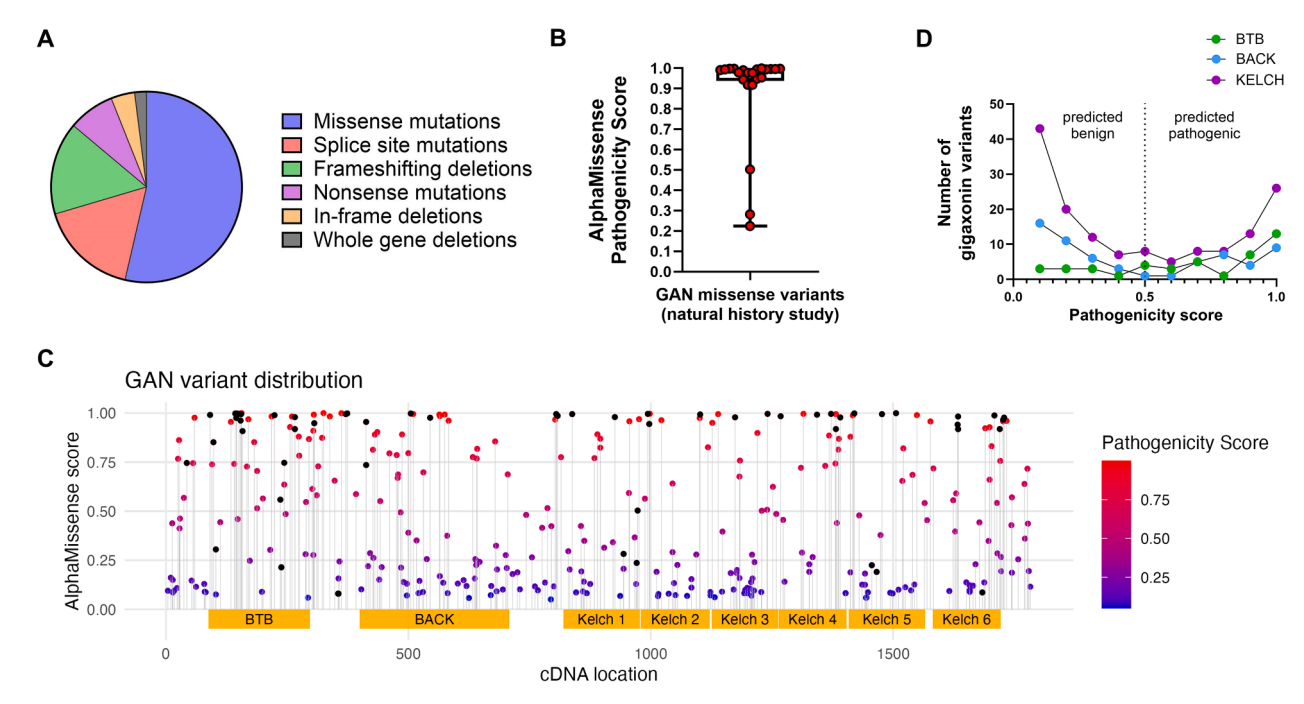
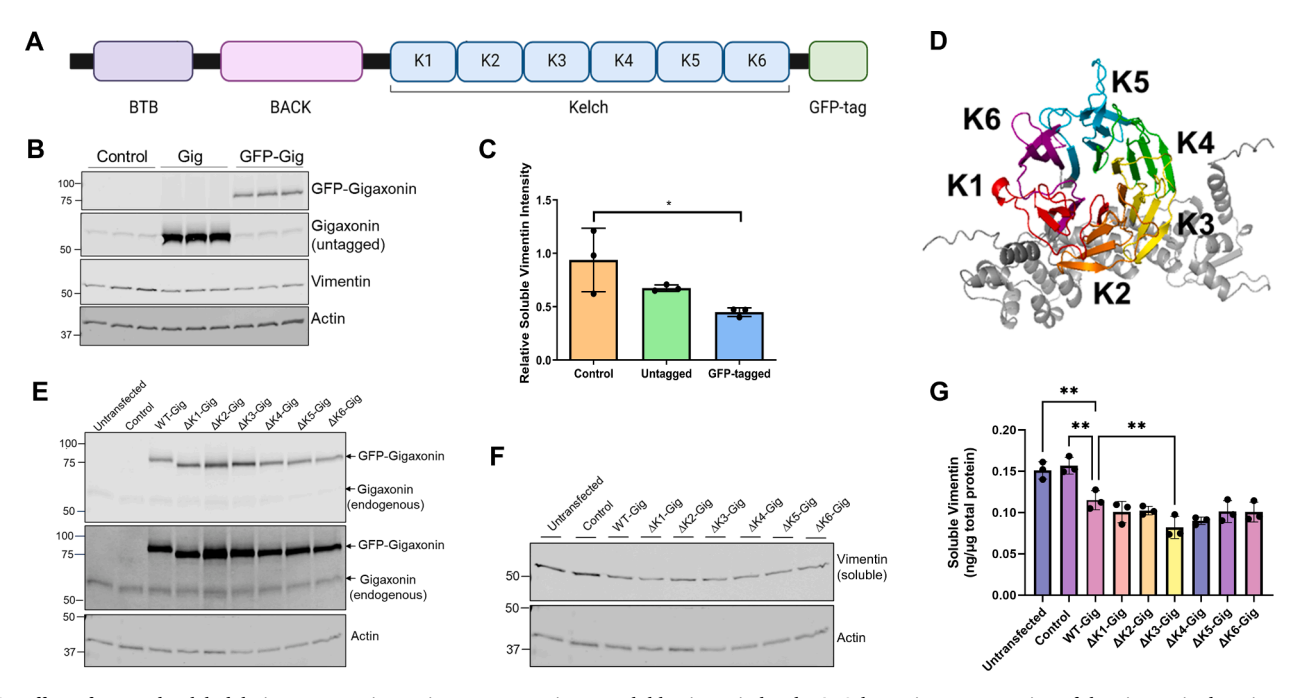


Fig. 1. Pathogenicity of GAN missense variants across the gigaxonin protein domains. A. Missense mutations are the most common GAN variants; based on a genetic analysis of the GAN natural history study cohort in Bharucha-Goebel et al., *Brain* 2021. B. AlphaMissense scores on known disease-causing GAN variants from the natural history study, as represented by box-and-whisker plot (n = 22; median score=0.9850). C. Missense GAN variants from ClinVar plotted by their respective cDNA location (x-axis) and AlphaMissense pathogenicity score (y-axis). Black dots represent known disease-causing GAN variants; from Bharucha-Goebel et al., *Brain* 2021 and Lescouzeres & Bomont, *Front Physiol* 2020. Blue and red dots represent variants where blue is predicted benign and red is predicted pathogenic. Yellow boxes represent the gigaxonin functional domains BTB, BACK, and Kelch, as defined in UniProt (ID: Q9H2C0). D. Frequency distribution plot of AlphaMissense pathogenicity scores of gigaxonin variants, according to the protein domain affected: BTB, green; BACK, blue; KELCH; magenta.



**Fig. 2.** Effect of WT and Kelch deletion mutant gigaxonin over-expression on soluble vimentin levels. **A.** Schematic representation of the gigaxonin domains and the location of the turbo-GFP tag at the C-terminus. **B.** Immunoblot for wild type GFP-tagged and untagged gigaxonin and the effect of their overexpression on TritonX-soluble vimentin levels in HEK293 cells; actin serves as a loading control. **C.** Quantification of the vimentin immunoblots from panel B. \*p < 0.05; one-way ANOVA. **D.** AlphaFold model of gigaxonin showing the predicted beta propeller structure and location of each Kelch motif that compose the gigaxonin Kelch domain. **E.** Immunoblots of GFP-gigaxonin and endogenous gigaxonin in cells expressing WT or Kelch deletion mutants. Two exposures of the same membrane are shown to visualize the relative levels of the endogenous vs. the over-expressed GFP-tagged form. **F.** Immunoblot of TritonX-soluble vimentin in HEK293 cells transfected with WT and Kelch deletion mutants of gigaxonin. **G.** Quantitative vimentin ELISA of soluble vimentin. \*\*p < 0.01; one-way ANOVA compared to WT-Gig group.

in HEK293 cells and its expression is unaffected by the presence of the ectopic constructs (Fig. 2E). To determine whether the IF degradation function of gigaxonin is compromised by the removal of each individual motif, we next measured TritonX-soluble vimentin protein. Soluble vimentin was reduced similarly in the deletion mutants compared to

WT-Gig based on western blot analysis (Fig. 2F). A quantitative ELISA assay confirmed the western blot results and further revealed that  $\Delta$ K3-Gig is more active in degrading soluble vimentin compared to WT-Gig (Fig. 2G). Overall, these results show that the individual Kelch motifs are dispensable for the ability of gigaxonin to target soluble

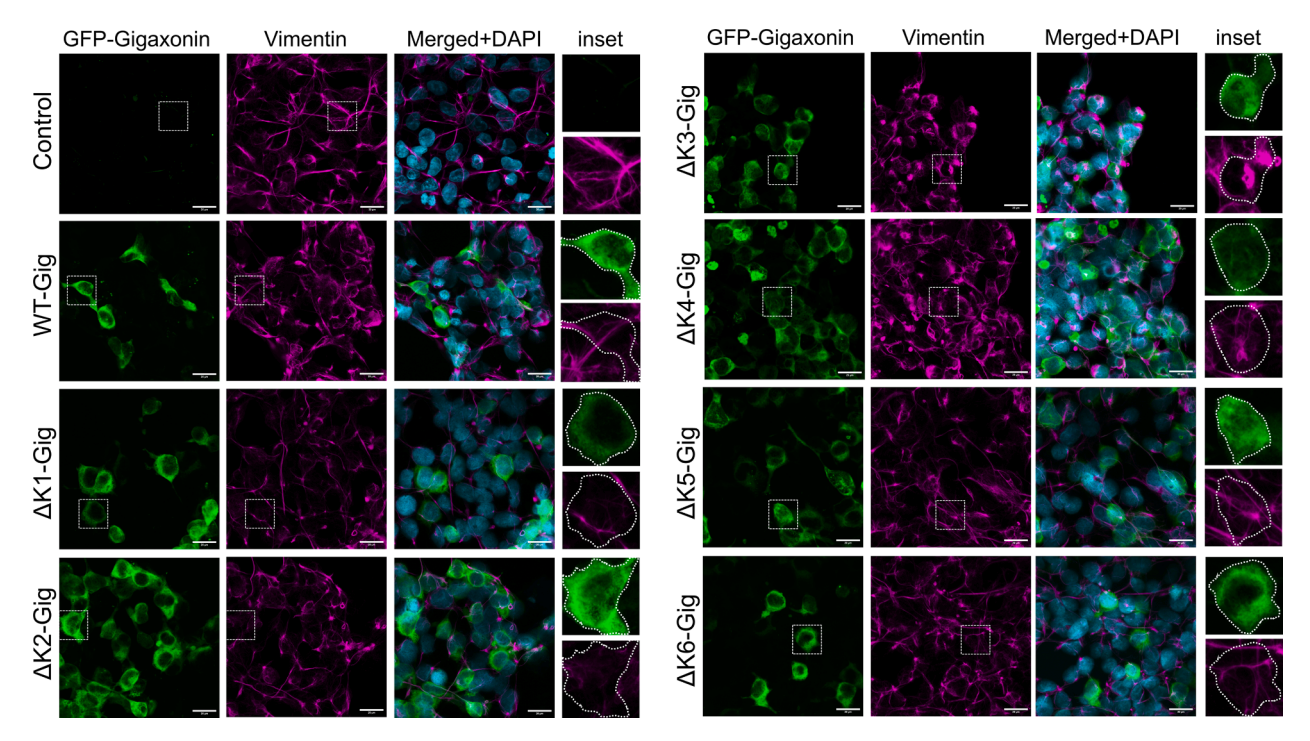


Fig. 3. Vimentin filament morphology in HEK293 cells expressing WT and Kelch deletion mutants of gigaxonin. Immunofluorescence analysis of GFP-gigaxonin (green), vimentin (magenta), and DAPI (cyan) in HEK293 cells transfected with GFP-tagged WT gigaxonin (Gig) and Kelch motif deletion mutants ( $\Delta$ K1-K6); Lipofectamine-only condition serves as transfection control. Scale bar=  $20\mu$ m. Boxed areas are enlarged to show the filament phenotypes in transfected cells.

vimentin for degradation.

## 2.3. Deletion of the gigaxonin Kelch 3 or Kelch 4 motif promotes vimentin bundling

Next, we analyzed the morphology of vimentin IFs in HEK293 cells transfected with the WT gigaxonin and the Kelch deletion constructs. The organization of the vimentin filament network was similar across the transfections, except for cells expressing  $\Delta$ K3, and to a lesser extent  $\Delta$ K4, where vimentin appeared thick and bundled (Fig. 3). To quantify the bundling phenotype, we analyzed the vimentin filaments using the Local Thickness tool in Fiji (ImageJ2). This analysis provided a heat map image (Supplemental Fig.1) and a histogram of pixel counts binned according to grey value intensity (Supplemental Table 1). Representative images of normal and bundled filaments are shown in Fig. 4A. where the filaments are colored based on their focal signal intensity. Analysis of all 8 conditions revealed significant differences between Lipofectamine-only control and WT-Gig and between WT-Gig and ΔK3-Gig (Fig. 4B). The  $\Delta$ K3 mutant-transfected cells contained significantly more thick vimentin bundles with intensity > 40 (Fig. 4C). Although not statistically significant,  $\Delta K4$  also showed an increase in the presence of thick vimentin bundles (Fig. 4C). Since IF aggregation is a feature commonly observed in cells impacted by GAN-causing gigaxonin mutations (Mahammad et al., 2013), the data allude to the possibility that, despite being dispensable for degrading a pool of soluble vimentin, the Kelch 3 motif may be involved in other mechanisms that regulate the vimentin filament structure.

### 2.4. The Kelch 3 and Kelch 4 motifs mediate gigaxonin protein interactions

Seeking to uncover new interactions of gigaxonin that are dependent upon the Kelch 3 and Kelch 4 motifs, we conducted a mass spectrometry analysis on HEK293 cells after GFP pulldowns from triplicate controltransfected (Lipofectamine only) cells, and cells overexpressing GFP vector, GFP-WT-gigaxonin, GFP-ΔK3-gigaxonin and GFP-ΔK4-gigaxonin. This analysis identified 73 interactions that were significantly changed by the K3 deletion and 44 interactions that were significantly changed by the K4 deletion relative to WT-Gig (Supplemental Table 2). Deletion of K3 primarily led to increased association between gigaxonin and a number of chaperones, mitochondrial proteins, and ubiquitininteracting proteins (Fig. 5A-B). Notably, increased interactions were observed with several ubiquitin ligases, including STUB1, UBE2M, UBE2J1, TRIM38 and the ubiquitin ligase regulator BAG2; deubiquitinases VCPIP1 and OTUB1; and the ubiquitin-binding proteins FAF1 and UBAC2 (Fig. 5B). A large number of mitochondrial proteins associated more strongly with  $\Delta$ K3-Gig, most notably NME3, a known regulator of mitophagy and mitochondrial dynamics (Fig. 5B).

Many of the interactions altered by K3 deletion were also affected by K4 deletion, but to a lesser degree, as visualized by the log-fold-change (LFC) values (Fig. 5C). Strikingly, both the Kelch 3 and Kelch 4 deletion eliminated the association between gigaxonin and a single protein – the NudC domain-containing protein (NUDCD3) (Fig. 5A, Fig. 5C). Using immunoblot analysis, we confirmed that the NUDCD3-gigaxonin interaction was eliminated in  $\Delta$ K3-Gig and  $\Delta$ K4-Gig (Fig. 5D). To assess whether NUDCD3 associates with vimentin aggregates in a GAN-relevant context, we analyzed two GAN patient fibroblast lines (B15–100.1 and B16–02) that we previously described (Battaglia et al., 2023). The B15–100.1 line carries a missense mutation E486K (Kelch 5)

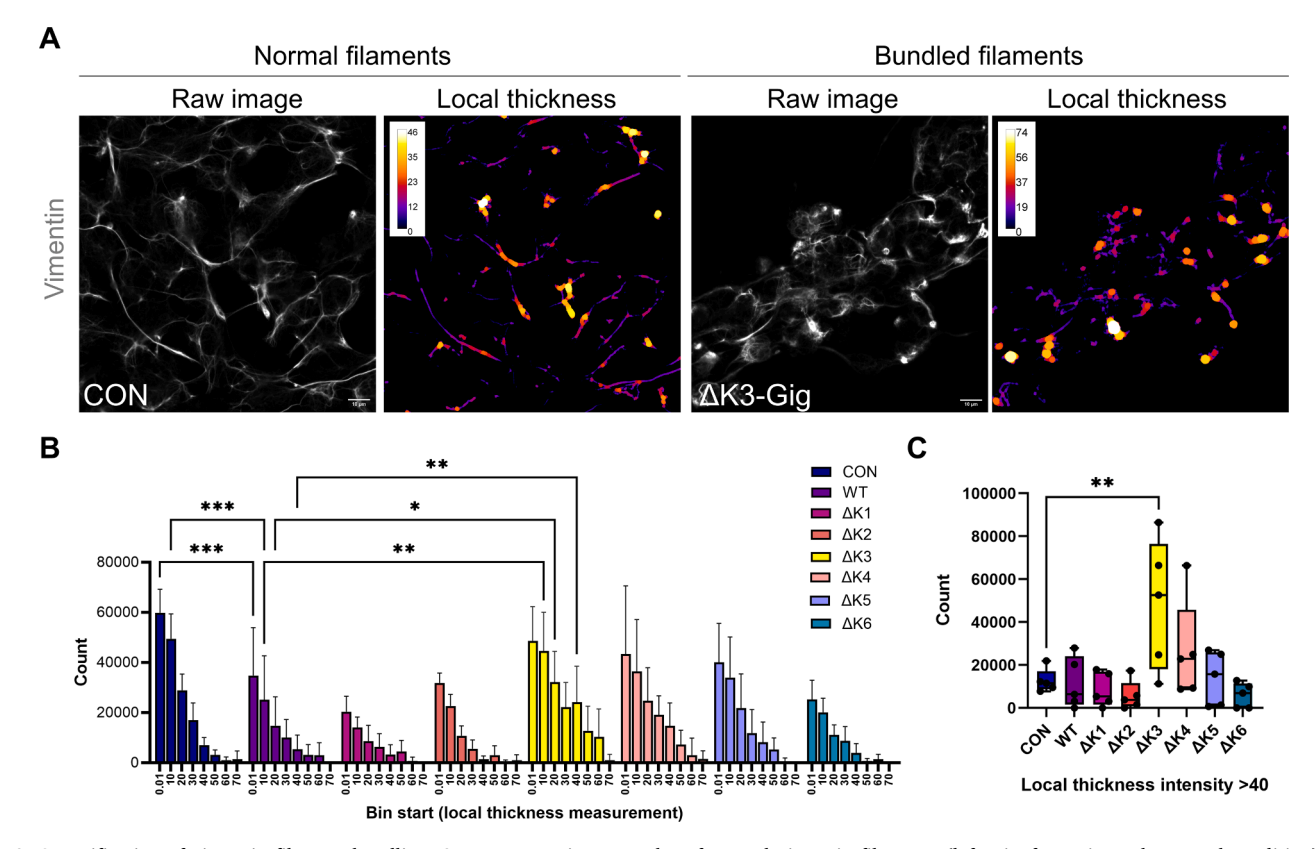


Fig. 4. Quantification of vimentin filament bundling. A. Representative examples of normal vimentin filaments (left; Lipofectamine-only control condition) and bundled vimentin filaments (right;  $\Delta$ K3-Gig transfection) in HEK293 cells. Shown side-by-side are the raw images and local thickness - analyzed images with colors representing pixel intensity in grey value. Scale bars= 10  $\mu$ m. B. Histograms of local thickness intensity counts for each condition. \*p < 0.05; \*\*p < 0.01; \*\*\*p < 0.001; two-way ANOVA. C. Box-and-whisker plot of combined counts for pixels with intensity value > 40 for each condition. \*\*p < 0.01; one-way ANOVA.

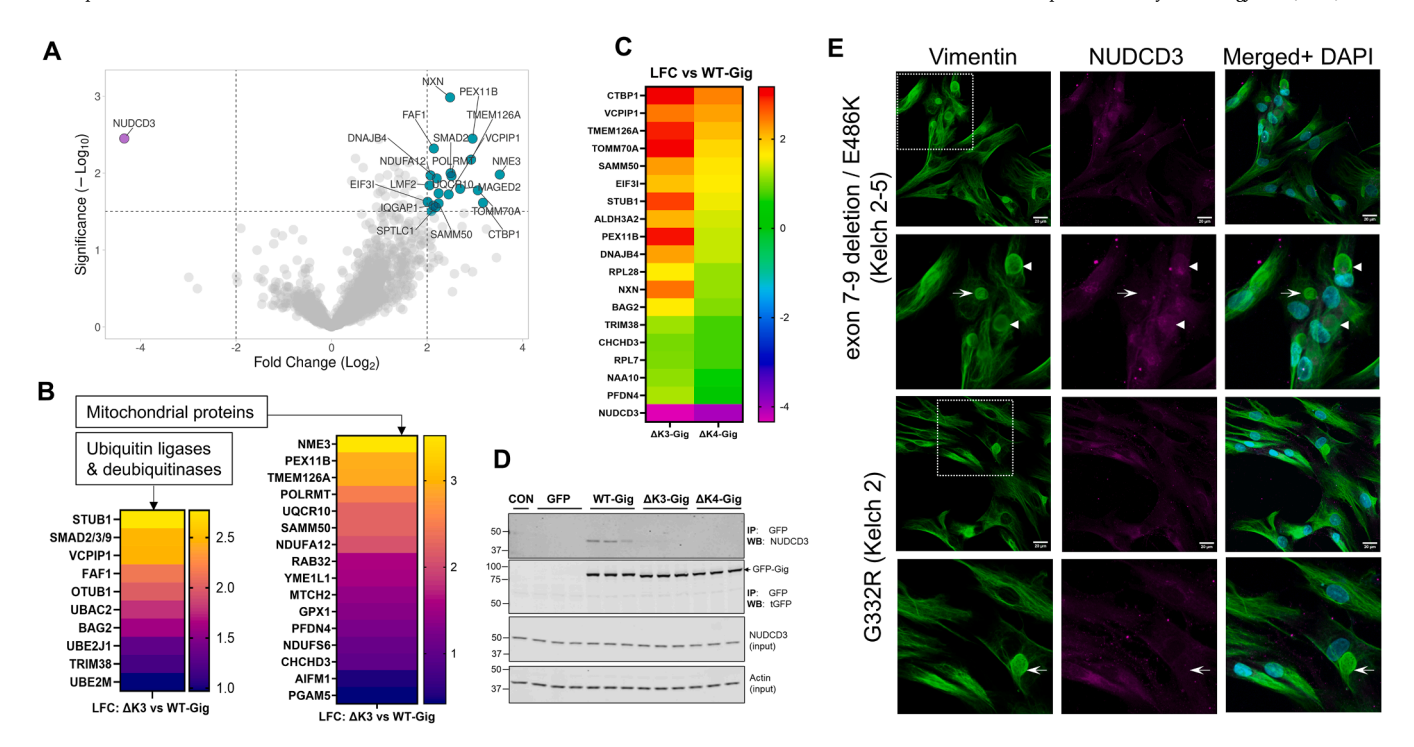


Fig. 5. Effect of gigaxonin Kelch 3 and Kelch 4 deletion on gigaxonin protein interactions. A. Volcano plot of protein interactors of ΔK3-gigaxonin that were significantly changed from WT-gigaxonin, based on mass spectrometry analysis on GFP-Gig pulldowns. Cyan dots represent increased interactions; magenta dot represents decreased interaction. B. Heat maps of the two major categories of differentially interacting gigaxonin partners in the absence of the Kelch 3 motif. Left map shows ubiquitin ligases/deubiquitinases and right map shows mitochondrial proteins (selected out of 73 statistically significant proteins detected in the ΔK3-Gig pulldown relative to WT-Gig; full list in Supplemental Table 2). C. Heat map of gigaxonin interactors that were significantly changed in K3 and K4 compared to WT-Gigaxonin. D. Immunoblot analysis of NUDCD3 and GFP-Gig in GFP pulldowns on cell lysates from Lipofectamine control, GFP empty vector and GFP-gigaxonin conditions (WT, ΔK3 and ΔK4). Input lanes show total levels of NUDCD3 and actin (loading control) in the lysates. E. Immunofluorescence analysis of vimentin and NUDCD3 localization in two GAN patient fibroblasts (B15–100.1; top and B16–02; bottom). Boxed areas denote magnified images. Arrowheads point to colocalized signal between vimentin aggregates and NUDCD3. Scale bar = 20 μm.

and a deletion of Exons 7–9, affecting part of Kelch 2 and 5, and all of Kelch 3-4. The GAN patient line B16–02 carries a homozygous missense mutation G332R, affecting Kelch 2. NUDCD3 was expressed at a low level in both lines, and appeared to co-localize with some vimentin aggregates, particularly in the B15–100.1 line (Fig. 5E, arrowheads), but there were also examples where the two did not co-localize (Fig. 5E, arrows).

While the nature of the gigaxonin-NUDCD3 interaction and its relevance to IF aggregation phenotypes in GAN cells remains to be determined, structural modeling confirmed the association between the two proteins. Specifically, an AlphaFold prediction model revealed gigaxonin interacting with NUDCD3 via its Kelch domain (Fig. 6A-B), while the binding was eliminated by the removal of Kelch 3 (Fig. 6C). Whereas Kelch 4 removal did not result in loss of binding, the model predicted a different binding mode for this construct (Fig. 6D). These data reveal a potential link between the loss of gigaxonin-NUDCD3 interactions with impaired IF proteostasis.

#### 3. Discussion

Our results revealed the importance of the gigaxonin Kelch 3 motif for the maintenance of proper protein interactions and vimentin filament structure. While it has been previously reported that the Kelch domain on gigaxonin interacts with IF proteins to promote proteasomal turnover (Johnson-Kerner et al., 2015), the contributions of the individual Kelch motifs to this degradation process have not been elucidated. Advancing knowledge of domain-specific functions for gigaxonin is essential to understand the high pathogenicity predictions for variants within the different protein segments, as this is translationally relevant to GAN disease-causing variants.

The functional significance of the interaction between gigaxonin and NUDCD3 requires further study, especially in cells of the nervous system, such as neurons and astrocytes, which are severely impacted by the mutations. Our finding of gigaxonin/NUDCD3 interaction loss suggests a potential new disease mechanism associated with the gigaxonin deficiency present in GAN. Currently, there is limited mechanistic information about the molecular chaperone NUDCD3 (also known as NudCL). However, it has been reported to interact with both dynein-1 and dynein-2 motor proteins via the dynein intermediate chain (DIC) (Asante et al., 2014). In the absence of NUDCD3, HeLa cells exhibited impaired mitosis and subsequent cell death, dynein complex mislocalization, and DIC aggregation and degradation, suggesting an important role for NUDCD3 in maintaining normal dynein function in the context of cell proliferation (Zhou et al., 2006). Interestingly, overexpression of NUDCD3 was also shown to have detrimental effects on the cell cycle, resulting in compromised mitosis, cytokinesis, and cell division (Cai et al., 2009). Loss of NUDCD3 in retinal pigment epithelial (RPE) cells led to decreased expression of a DIC protein specific to the dynein-2 complex and reduced ciliogenesis, likely due to defective transport between dynein-2 and the cilia (Asante et al., 2014). Further, mutations in dynein-2-associated DIC proteins led to diminished interactions with NUDCD3, which in turn contributed to the destabilization of both the DIC and overall dynein complex (Vuolo et al., 2018). Inhibition of NUDCD3 partially reduced dynein-mediated retrograde transport of mitochondria in rat hippocampal neurons while knockdown of NUDCD3 in conjunction with another NUD family member led to a nearly complete loss of transport (Shao et al., 2013).

It has been proposed that NUDCD3 functions as a chaperone to assist with proper folding of proteins with  $\beta$ -propellers, including numerous WD40-repeat proteins like the DIC proteins, and it has been reported to

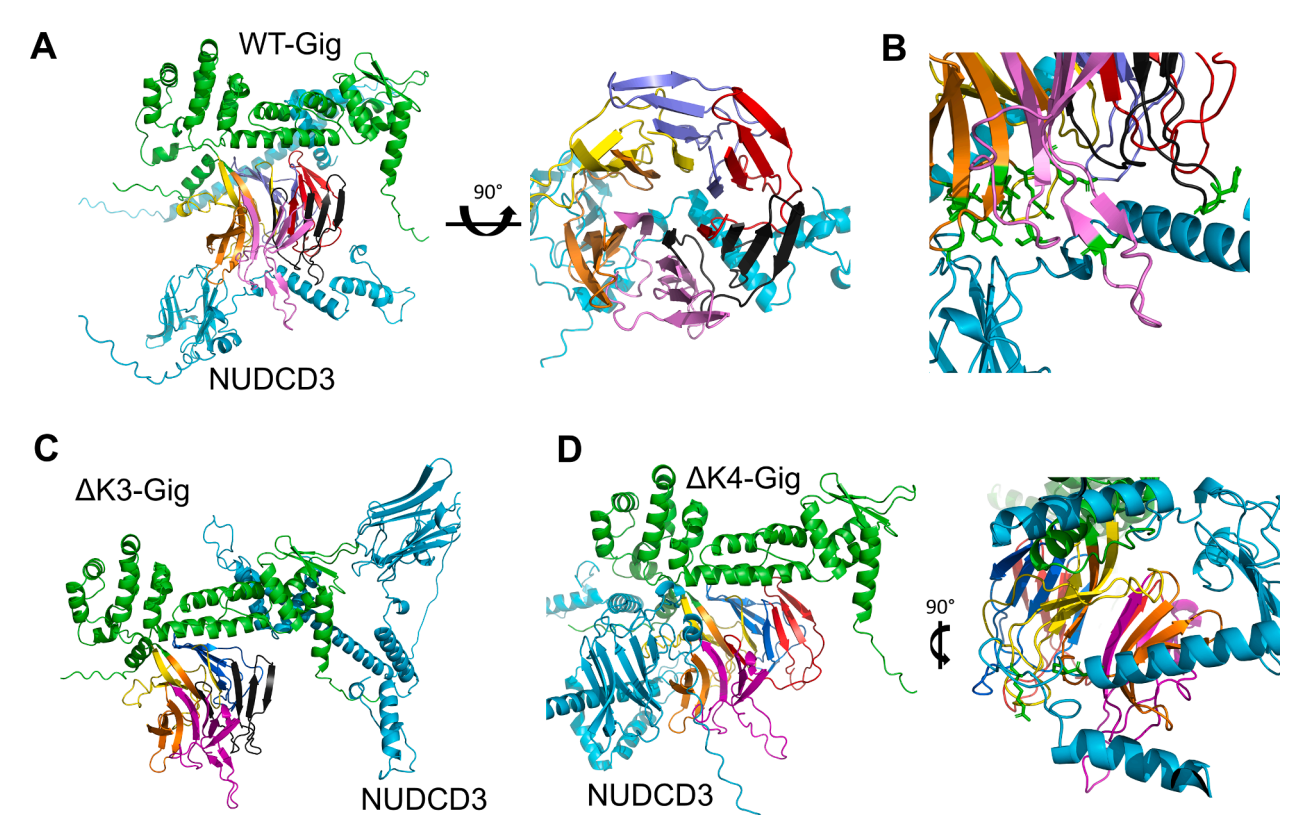


**Fig. 6.** AlphaFold 3 predicted model of gigaxonin interacting with NUDCD3. **A.** Gigaxonin is shown in green with the exception of the Kelch domain that is colored by motif: Kelch 1 (aa274–326, yellow), Kelch 2 (aa327–374, blue), Kelch 3 (aa376–421, red), Kelch 4 (aa422–468, black), Kelch 5 (470–522, purple), Kelch 6 (528–574, orange). Upon rotating the model 90 degrees, the classic beta-propeller organization of the Kelch repeat motifs becomes visible, showing the NUDCD3 (in cyan) interactions with specific Kelch motifs. **B.** Zoomed in image of AlphaFold 3 predicted model of gigaxonin (colored by Kelch motif as described above, interacting with NUDCD3 (cyan). Amino acids in the Kelch domain predicted to be within 3 Å of NUDCD3 are localized to Kelch 4–6 and are shown as green sticks. **C.** AlphaFold 3 predicted model of gigaxonin ΔKelch 3 (aa376–421) (green) interacting with NUDCD3 (cyan), with the remaining Kelch motifs colored as in panel A. With the removal of Kelch 3, NUDCD3 is no longer predicted to interact with the Kelch domain. **D.** AlphaFold 3 predicted model of gigaxonin ΔKelch 4 (aa422–468) (green) interacting with NUDCD3 (cyan), with the remaining Kelch motifs colored as in panel A. Without Kelch 4, NUDCD3 is predicted to adopt an entirely different conformation to interact with gigaxonin. This includes NUDCD3 interacting more with Kelch 1 (yellow), especially through its N-terminal (green sticks), which was not shown in the wild-type predicted model.

interact with other KLHL proteins (Taipale et al., 2014; Vuolo et al., 2018). Since the Kelch domain of gigaxonin is predicted to also form a β-propeller structure (Boizot et al., 2014), it is possible that NUDCD3 facilitates the proper folding and stabilization of the Kelch domain. Although we did not observe evidence of significant aggregation or degradation of the GFP-tagged  $\Delta$ K3 and  $\Delta$ K4 gigaxonin constructs, the loss of interaction with NUDCD3 may have led to variations in the folding pattern with downstream impacts on the roles for gigaxonin that are unrelated to IF protein turnover. Additional studies are needed to discern the binding mechanisms of NUDCD3 to gigaxonin to further perturb this association and study the resulting functional effects on gigaxonin. Interestingly, NUDCD3 is enriched in the nervous system (Fagerberg et al., 2014) and has been reported to interact with KLHL proteins that are highly expressed in the brain, involved in actin-binding and neuronal development (rather than participating in the UPS), and implicated in neurological conditions and brain tumors (Dhanoa et al., 2013; Shi et al., 2019). This highlights the importance of further studying the gigaxonin-NUDCD3 interaction in neurons, the most severely affected cell type in GAN, both under homeostatic and pathological conditions.

A recent study demonstrated that loss of gigaxonin led to impaired kinesin-1-mediated trafficking of vimentin in RPE cells and neurofilaments in dorsal root ganglion neurons, while transport of other cargo remained unaffected (Renganathan et al., 2023). Interestingly, direct binding of vimentin to kinesin-1 in gigaxonin knockout cells seemed to partly restore IF transport, suggesting that the interaction between IFs

and kinesin is disrupted when there is a loss of gigaxonin (Renganathan et al., 2023). It is not currently known if kinesin-1 directly or indirectly binds to IFs, or if this interaction incorporates gigaxonin as well. While the dynein complex has also been previously shown to transport neurofilament IFs (Uchida et al., 2009), potential trafficking defects associated with this motor protein in the context of GAN currently remain unknown.

Additional studies examining the effects of mutated forms of gigaxonin (missense or Kelch motif deletions), rather than a complete knockout, on kinesin or dynein mediated IF transport will help to elucidate whether defective IF trafficking is a result of gigaxonin's role as an E3 ligase adaptor or another function. Since cells expressing  $\Delta K3$ -Gig exhibited IF phenotypes reminiscent of those observed in GAN patient cells, it is possible that gigaxonin may play a larger role in IF transport mechanisms outside of regulating soluble IF protein turnover. However, the unexpected finding that deletion of the individual Kelch motifs did not impact soluble vimentin degradation suggests that mutated forms of gigaxonin may retain some functional activity when expressed in cells. In most GAN patients, gigaxonin is extremely low or absent, although the exact molecular mechanisms for gigaxonin loss in the case of missense mutations are not clear. Further studies are needed to discern if mutant forms of gigaxonin can be stabilized, for example by overexpressing NUDCD3 or another chaperone, and if they retain sufficient functional activity to degrade IFs in the most severely affected cell types.

Collectively, our cell biological data showed the induction of a GAN-

like IF phenotype in cells expressing Kelch 3 motif-deficient gigaxonin, while our proteomics profiling linked the loss of gigaxonin-NUDCD3 interactions with defective IF proteostasis, building upon recent findings that gigaxonin regulates IF transport (Renganathan et al., 2023). The findings reveal a potential new mechanism behind the pathologic effect of gigaxonin deficiency and may help to explain high pathogenicity predictions from the structure-based analysis of gigaxonin variants affecting specific segments of the Kelch domain.

#### 4. Materials and methods

#### 4.1. Antibodies

The following primary antibodies and concentrations were utilized: mouse anti-tGFP (Origene, OT12H8, IF: 1:200–1:350), rabbit anti-Gigaxonin (Novus, NBP1–49924, WB: 1:250–1:500, IF: 1:100), rabbit anti-Vimentin (Cell Signaling Technology, D21H3, WB 1:1000, IF 1:200), mouse anti-Actin (Santa Cruz, SPM161, WB 1:1000), and mouse anti-NUDCD3 (Santa Cruz, WB: 1:200, IF: 1:150). The following secondary antibodies and concentrations were utilized: IRDye 800CW goat anti-rabbit IgG (LI-COR, WB 1:5000), IRDye 680RD donkey anti-mouse IgG (LI-COR, WB 1:5000), and Alexa 488-, Alexa 568-, and Alexa 594-conjugated goat anti-mouse and anti-rabbit antibodies (Invitrogen, IF 1:500).

## 4.2. Site-directed mutagenesis, transformation, and preparation of pCMV6-AC-GFP vector, wild type gigaxonin, and gigaxonin Kelch motif deletion constructs

Mutagenesis of GFP-tagged wild-type gigaxonin (pCMV6-AC-GFP vector; Origene) was conducted with the In-Fusion® Snap Assembly kit (Takara Bio) in accordance with manufacturer's instructions to generate the following domain deletions (see table below for primers designed using primer design tool from Takara Bio): Kelch 1, Kelch 2, Kelch 3, Kelch 4, Kelch 5, and Kelch 6. Transformation for GFP-tagged gigaxonin wild type and Kelch 1-6 deletion constructs was conducted using Stellar Competent Cells (Takara Bio) provided with the In-Fusion® Snap Assembly kit. The cell suspension from the transformation was spread onto an ampicillin agar plate, then incubated overnight at 37°C. Colonies were individually picked and inoculated overnight at 37°C shaking at 225 RPM in LB media (Fisher Scientific) with ampicillin (100 µg/µL). Plasmid DNA was extracted using the PureLinkTM Quick Plasmid Miniprep kit (Invitrogen) and submitted for Sanger sequencing to check for desired and potential off-target changes in the vector, coding region of gigaxonin, or GFP-tag. After confirming the sequences, previously inoculated cell suspension was added to LB media with ampicillin (100 µg/µL), then incubated overnight at 37°C shaking at 225 RPM. Plasmid DNA was extracted using either the ZymoPURE II Plasmid Midiprep Kit (Zymo) or the QIAfilter Plasmid Midi Kit (Qiagen) to generate 100 ng/ $\mu L$  and 500 ng/ $\mu L$  transfection stocks. Additional transformations for the pCMV6-AC-GFP vector (Origene), untagged wild type gigaxonin (pCMV6-XL4 vector; Origene), and GFP-tagged gigaxonin wild type (pCMV6-AC-GFP vector; Origene), Kelch 3 deletion, and Kelch 4 deletion constructs was conducted using XL1-blue supercompetent cells (Agilent Technologies), which were utilized in accordance with product instructions. Plasmid DNA was extracted to generate 100 ng/μL and 500 ng/μL transfection stocks as described.

#### 4.3. Site-directed mutagenesis and sequencing primers

Primer Name	Sequence
Human GAN Kelch 1 deletion F	ACTCTGAGTTTTTGTTTGTATTCGGGGGCC
Human GAN Kelch 1 deletion R	ACAAAAACTCAGAGTAGCCCCGGGG
Human GAN Kelch 2 deletion F	CAGAAGGAATGCTGTACATTTTGGGAGGAGAGG
Human GAN Kelch 2 deletion R	ACAGCATTCCTTCTGCTGAGAGAACTCC
Human GAN Kelch 3 deletion F	ATGGGATGAAAATCTACGCCATGGGTGGAGG
Human GAN Kelch 3 deletion R	AGATTTTCATCCCATCTATCTCCACAATTCCG
Human GAN Kelch 4 deletion F	TGAAAAAGGAGCTGTATGTGTTTTGGGGG
Human GAN Kelch 4 deletion R	ACAGCTCCTTTTTCATAGCTGCATAGCAGCCG
Human GAN Kelch 5 deletion F	CTATGGAGGTACCTATAGGAGCCAGTATTTATG
Human GAN Kelch 5 deletion R	TAGGTACCTCCATAGCAACTCCACAGG
Human GAN Kelch 6 deletion F	TAGGAGCCATTGCGAATTGCAAGCTTTTCCG
Human GAN Kelch 6 deletion R	TCGCAATGGCTCCTATAGGTACAGCTCC
Human GAN Kelch 5&6 deletion F	GACCATGGTCAGAAAGATCGGC
Human GAN Kelch 6 deletion R	CCAGCTCGAACTCCACGCC
Human GAN F1	CAGCCCGTACATCAGGACAA
Human GAN R1	CTGATCTGCCCACTGAAGATGT
Human GAN F2	AGTGCATCGTGACTGTTGGT
Human GAN R2	TCCAAAGCTGCCTGTTAGGG

#### 4.4. Cell lines, cell culture, and transfection of gigaxonin mutants

HEK293 cells were cultured in MEM (ThermoFisher Scientific) with 10 % FBS (Genesee Scientific, Lot: P093156 & Lot: P121400) and 1 % penicillin/streptomycin (pen/strep; ThermoFisher Scientific). GAN patient fibroblasts were thawed initially in DMEM (Gibco) in 20 % FBS and 1 % pen/strep and passaged every 3–4 days with 0.05 % Trypsin-EDTA (Gibco), and after a few passages, the cells were maintained in 10 % FBS media.

HEK293 cells were plated on 10 cm plates or 8-well chamber slides at 40–60 % confluency in MEM + 10 % FBS media (no antibiotics). The following day, the cells were transfected with the pCMV6-AC-GFP vector, gigaxonin wild type construct, and/or the Kelch deletion constructs plus Lipofectamine 3000 and p3000 reagents that were utilized in accordance with product instructions (ThermoFisher Scientific). A Lipofectamine/p3000 only condition was utilized as well as an untransfected control. Media was changed to MEM + 10 % FBS + pen/strep media 4–6 h after transfection, and cells were harvested for immunoprecipitation (see below for details) or fixed for imaging (see below for details on immunostaining procedures) at the 48-hour time point.

For transfection experiments for immunoblot analysis, HEK293 cells were plated on 6-well plates at 80 % confluency in MEM + 10 % FBS media (no antibiotics) with transfection reagents, including gigaxonin wild type and Kelch motif deletion plasmids, p3000, and Lipofectamine 3000. Media was changed to MEM + 10 % FBS + pen/strep media 4–6 h after transfection, and cells were harvested in TritonX-100 buffer at the 72-hour time point and separated into TCL, detergent soluble, and detergent insoluble fractions (see below for details on preparation of protein lysates).

#### 4.5. Preparation of protein lysates and immunoblotting

For immunoblot analysis, transfection lysates were prepared by adding 300-600 µL cold TritonX-100 buffer (1 % Triton X-100, 0.5 M EDTA, PBS, ddH<sub>2</sub>O) with protease/phosphatase inhibitors (Halt™ Protease & Phosphatase Inhibitor Cocktail, EDTA-free, 100X; ThermoFisher Scientific), scraping the cells with the plates on ice, and transferring the cell suspension into Eppendorf tubes; 10 % of cell suspension was reserved as the TCL fraction and resuspended in an equal volume of hot 2X Novex<sup>TM</sup> Tris-Glycine SDS Sample Buffer (Thermo Fisher Scientific). The cell suspension was spun down in a tabletop centrifuge at 14,000xg for 10 min at 4°C to separate the detergent soluble and insoluble fractions, the supernatant was transferred to a new tube (detergent soluble fraction), then the remaining pellet (detergent insoluble fraction) was resuspended in hot sample buffer. All samples resuspended in with SDS sample buffer were heated at 95°C for 5 min and reduced with 5 % 2mercaptoethanol (Sigma) as needed. Total protein concentration for the detergent soluble fractions were measured with Pierce<sup>TM</sup> BCA Protein Assay Kit (Thermo Fisher Scientific) and Biotek Synergy HT plate reader according to manufacturer's instructions; total protein concentrations were calculated from the recorded absorbance values. The concentrations were used to calculate 300 ng/uL stocks; the samples were diluted with TritonX-100 buffer (+protease/phosphatase inhibitors). Working stocks were prepared by adding an equal volume of hot SDS sample buffer to each sample, reducing with 5 % 2-mercaptoethanol, and heating at 95°C for 5 min.

For immunoblotting, samples were loaded with equal volumes and protein amounts and separated on 10 % or 4–20 % Novex<sup>TM</sup> Wedge-Well<sup>TM</sup> Tris-Glycine gels (Thermo Fisher Scientific) for 40 min at 225 V or 80-90 min at 120 V and transferred at 40 V overnight at  $4^{\circ}\text{C}$  onto nitrocellulose membranes. Gels were stained with Coomassie and destained following each transfer to verify normalization. The membranes were blocked in 5 % non-fat milk (NFM) dissolved into 0.1 % tween 20/PBS (PBST) at room temperature for 30–60 min. The membranes were incubated in primary antibodies diluted in 5 % NFM/PBST at room temperature for 1 h (see concentrations above), then washed 3x with PBST for 5 min each. The membranes were incubated with secondary antibodies diluted in 5 % NFM/PBST at room temperature for 1 h (see concentrations above), washed 3x with PBST and 1x with PBS for 5 min each, then scanned with a LI-COR Odyssey CLx machine.

#### 4.6. Immunoprecipitation with anti-GFP magnetic beads

For the immunoprecipitation (IP) experiment, transfection lysates were washed with HBSS and lysed in 1 mL cold TritonX-100 buffer (1 % Triton X-100, 0.5 M EDTA, PBS, ddH<sub>2</sub>O) with protease/phosphatase inhibitors (Halt™ Protease & Phosphatase Inhibitor Cocktail, EDTAfree, 100X; ThermoFisher Scientific). The cell suspension was spun down in a tabletop centrifuge at 14,000xg for 20 min at 4°C to separate the detergent soluble and insoluble fractions, and the supernatant was transferred to a new tube (detergent soluble fraction). Total protein concentration for the detergent soluble fractions were measured with Pierce™ BCA Protein Assay Kit (Thermo Fisher Scientific) and Biotek Synergy HT plate reader according to manufacturer's instructions; total protein concentrations were calculated from the recorded absorbance values. The concentrations were used to calculate 1  $\mu g/\mu L$  stocks; the samples were diluted with TritonX-100 buffer (+protease/phosphatase inhibitors). To obtain an input immunoblot for comparison to the IP, a fraction of each 1 µg/µL stock was resuspended with an equal volume of hot SDS sample buffer, reducing with 5 % 2-mercaptoethanol, and heating at 95°C for 5 min. Samples were loaded into gels at equal volumes and protein amounts and SDS-PAGE/immunoblot procedures were conducted as described above.

ChromoTek TurboGFP-Trap Magnetic Agarose beads (Proteintech) were utilized for immunoprecipitation (IP) of GFP-tagged vector, gigaxonin wild type, and gigaxonin Kelch 3 and 4 deletion constructs in

accordance with product instructions. In brief, the beads were equilibrated with 3x washes with TritonX-100 buffer (1 % Triton X-100, 0.5 M EDTA, PBS, ddH2O) with protease/phosphatase inhibitors (Halt™ Protease & Phosphatase Inhibitor Cocktail, EDTA-free, 100X; Thermo Fisher Scientific); washes were manually removed when beads were separated using a magnetic rack. Following equilibration, detergent soluble 1 µg/ μL stocks were loaded onto magnetic beads and incubated overnight at 4°C while rotating. Following incubation, the supernatant was removed, the beads were washed 3x with TritonX-100 buffer (no inhibitors), then 20 % of the IP was transferred for elution with hot SDS sample buffer and heated at 95°C for 10 min. These samples were loaded into gels at equal volumes and SDS PAGE/immunoblot procedures were conducted as described above. The remaining IP was washed 3x with 50 mM Ammonium Bicarbonate (pH 7.8), then the captured protein was eluted in 50 mM Ammonium Bicarbonate (pH 7.8) for mass spectrometrybased proteomics analysis (described below).

#### 4.7. Immunofluorescence and imaging

HEK293 cells or GAN fibroblasts were rinsed with PBS and fixed in methanol at  $-20^{\circ}\mathrm{C}$  for 15 min, washed 2x with PBS for 5 min each, and incubated in blocking buffer (2.5 % Bovine Serum Albumin (Sigma), 2 % normal goat serum (ThermoFisher Scientific), PBS) at room temperature for 1 h. Cells were incubated with primary antibodies at room temperature for 1–2 h or overnight at 4°C, followed by 3  $\times$  5-minute PBS washes, then incubated with Alexa Fluor-conjugated secondary antibodies at room temperature for 1 h and washed 3x with PBS for 5 min each. Finally, cells were incubated in DAPI (Invitrogen), washed 2x with PBS for 5 min each, and mounted in Fluoromount-G (SouthernBiotech) overnight. Cells were imaged on Zeiss 880 confocal laser scanning microscope using a 63x oil immersion objective.

#### 4.8. Quantitative vimentin ELISA

TritonX-100 detergent soluble fractions for HEK293 cells transfected for 72 h with the wild type gigaxonin and Kelch deletion constructs, as well as untransfected and Lipofectamine3000 control samples, were analyzed using a vimentin ELISA (Cell Signaling Technology; Cat: 87105). The ELISA did not come with vimentin standards, so purified recombinant vimentin (gift from Dr. Harald Herrmann) of a known concentration was used and serially diluted to generate a standard range (in ng; 0.015, 0.03, 0.06, 0.12, 0.24, 0.49); standard curve concentrations were optimized to fall within the absorbance values measured by BioTek Cytation 5 plate reader. The 300 ng/µL stocks were utilized to generate 50 ng/µL samples (sample concentrations optimal for the standard curve were optimized in prior experiments), and the vimentin ELISA was performed in accordance with the manufacturer's instructions. The absorbance values for each sample were averaged across three technical replicates, then vimentin concentration (in ng) was calculated based on a standard curve and normalized to total protein concentration per sample (in µg).

#### 4.9. Mass spectrometry-based proteomics analysis

GFP-tagged gigaxonin immunoprecipitation samples were prepared as described above and stored in 50 mM Ammonium Bicarbonate (pH 7.8), then submitted for mass spectrometry-based proteomic analysis. In brief, on-bead tryptic digestion was performed, followed by peptide extraction and C18 desalting cleaning. Each sample was analyzed by LCMS/MS using the Thermo Easy nLC 1200-QExactive HF. The data were processed using MaxQuant (v1.6.15.0) – the data were searched against the Uniprot Human database (~20,000 sequences), a common contaminants database (~250 sequences), and gigaxonin sequences. The MaxQuant results were filtered and analyzed in Perseus, and reverse hits and proteins with 1 peptide (single hits) were removed. Perseus was used for imputation, log2 fold change and p-value calculations.

#### 4.10. Data analysis and statistics

AlphaMissense pathogenicity scores (Cheng et al., 2023) were obtained for all *KLHL16/GAN* gene coding missense variants classified as uncertain significance, likely pathogenic, or pathogenic in the NIH ClinVar database (Landrum et al., 2018) and for the variants reported from patient cohorts (Bharucha-Goebel et al., 2021; Lescouzeres and Bomont, 2020). Variants were plotted by cDNA location and Alpha-Missense pathogenicity score with each dot representing a *KLHL16/GAN* gene variant based on cDNA change. The dots are color-coded by pathogenicity score with blue as predicted to be benign and red predicted as pathogenic, and the black dots are variants that were found in a patient cohort. Yellow boxes represent the functional domains of gigaxonin (BTB, BACK, and Kelch 1–6 motif repeats) as defined by UniProt (UniProt, 2023) (entry code for human gigaxonin: Q9H2C0). Additional graphical data were generated with GraphPad Prism.

Image Studio version 5.2 (LI-COR) was used to perform densitometry on the immunoblot for soluble vimentin, and the relative intensities were analyzed by the GraphPad Prism software using one-way ANOVA. The ELISA results for the untransfected, Lipofectamine3000, wild type gigaxonin, and Kelch 1–6 deletion conditions were analyzed using one-way ANOVA via GraphPad Prism.

Quantification of vimentin bundling: For each condition (Lipofectamine control, WT-Gig and the six Kelch deletions  $\Delta$ K1- $\Delta$ K6-Gig) we quantified 5 confocal single slice images using the 'Local Thickness (complete process)' measurement in Fiji (ImageJ2) to determine pixel intensities (gray values). The intensities are reported visually as a heat map (Supplemental Fig.1) and numerically in histogram form (raw data in Supplemental Table 1). For the analysis, vimentin images were first converted to 8-bit and the local thickness settings used were: threshold= 64; bins= 10; pixel range: Xmin= 0.01; Xmax= 100; Ymax=auto.

All graphical data were generated with GraphPad Prism. The proteomics data were analyzed using the DAVID bioinformatics resource (Sherman et al., 2022), bar graphs and heat maps were generated with the GraphPad Prism software, and statistical analysis was performed via unpaired *t*-test, one-way, or two-way ANOVA, as specified in the figure legends.

#### CRediT authorship contribution statement

Phillips Cassandra L: Writing – review & editing, Writing – original draft, Visualization, Validation, Methodology, Investigation, Funding acquisition, Formal analysis, Conceptualization. Christina So: Writing – review & editing, Methodology, Investigation, Conceptualization. Gillis Meredith F: Writing – review & editing, Visualization, Methodology, Formal analysis. Jonathan Harrison: Writing – review & editing, Visualization, Methodology, Formal analysis. Chih-Hsuan Hsu: Writing – review & editing, Visualization, Investigation, Formal analysis. Diane Armao: Writing – review & editing, Writing – original draft, Supervision, Funding acquisition. Snider Natasha: Writing – review & editing, Writing – original draft, Visualization, Supervision, Resources, Project administration, Methodology, Funding acquisition, Formal analysis, Conceptualization.

#### Funding and additional information

This study was funded by Hannah's Hope Fund and NIH grants R21NS121578, R01NS136621 (NTS, DA), GM122741 (training award to CP), and AHA grant 24PRE1193707 (training award to CP). The content is solely the responsibility of the authors and does not necessarily represent the official views of the National Institutes of Health and the other sponsors.

#### **Declaration of Competing Interest**

The authors declare the following financial interests/personal

relationships which may be considered as potential competing interests: Natasha Snider reports financial support was provided by NIH, Hannah's Hope Fund, American Heart Association. If there are other authors, they declare that they have no known competing financial interests or personal relationships that could have appeared to influence the work reported in this paper.

#### Acknowledgments

The authors thank Dr. Laura Herring and Dr. Allie Mills affiliated with the UNC Metabolomics and Proteomics (MAP) Core for assistance with the mass spectrometry analysis. Microscopy was performed at the UNC Hooker Imaging Core Facility, supported in part by P30 CA016086 Cancer Center Core Support Grant to the UNC Lineberger Comprehensive Cancer Center.

#### Appendix A. Supporting information

Supplementary data associated with this article can be found in the online version at doi:10.1016/j.ejcb.2025.151508.

#### **Data Availability**

Data will be made available on request.

#### References

- Asante, D., Stevenson, N.L., Stephens, D.J., 2014. Subunit composition of the human cytoplasmic dynein-2 complex. J. Cell Sci. 127, 4774–4787.
- Battaglia, R., Faridounnia, M., Beltran, A., Robinson, J., Kinghorn, K., Ezzell, J.A., Bharucha-Goebel, D., Bonnemann, C., Hooper, J.E., Opal, P., Bouldin, T.W., Armao, D., Snider, N., 2023. Intermediate filament dysregulation in astrocytes in the human disease model of KLHL16 mutation in giant axonal neuropathy (GAN). Mol. Biol. Cell 34, mbcE23030094.
- Bharucha-Goebel, D.X., Norato, G., Saade, D., Paredes, E., Biancavilla, V., Donkervoort, S., Kaur, R., Lehky, T., Fink, M., Armao, D., Gray, S.J., Waite, M., Debs, S., Averion, G., Hu, Y., Zein, W.M., Foley, A.R., Jain, M., Bonnemann, C.G., 2021. Giant axonal neuropathy: cross-sectional analysis of a large natural history cohort. Brain 144, 3239–3250.
- Boizot, A., Talmat-Amar, Y., Morrogh, D., Kuntz, N.L., Halbert, C., Chabrol, B., Houlden, H., Stojkovic, T., Schulman, B.A., Rautenstrauss, B., Bomont, P., 2014. The instability of the BTB-KELCH protein Gigaxonin causes Giant Axonal Neuropathy and constitutes a new penetrant and specific diagnostic test. Acta Neuropathol. Commun. 2, 47.
- Bomont, P., Cavalier, L., Blondeau, F., Ben Hamida, C., Belal, S., Tazir, M., Demir, E., Topaloglu, H., Korinthenberg, R., Tuysuz, B., Landrieu, P., Hentati, F., Koenig, M., 2000. The gene encoding gigaxonin, a new member of the cytoskeletal BTB/kelch repeat family, is mutated in giant axonal neuropathy. Nat. Genet. 26, 370–374.
- Cai, Y., Yang, Y., Shen, M., Zhou, T., 2009. Inhibition of cytokinesis by overexpression of NudCL that is localized to the centrosome and midbody. Cell Res. 19, 1305–1308.
- Cheng, J., Novati, G., Pan, J., Bycroft, C., Zemgulyte, A., Applebaum, T., Pritzel, A., Wong, L.H., Zielinski, M., Sargeant, T., Schneider, R.G., Senior, A.W., Jumper, J., Hassabis, D., Kohli, P., Avsec, Z., 2023. Accurate proteome-wide missense variant effect prediction with AlphaMissense. Science 381, eadg7492.
- Dhanoa, B.S., Cogliati, T., Satish, A.G., Bruford, E.A., Friedman, J.S., 2013. Update on the Kelch-like (KLHL) gene family. Hum. Genom. 7, 13.
- Fagerberg, L., Hallstrom, B.M., Oksvold, P., Kampf, C., Djureinovic, D., Odeberg, J.,
  Habuka, M., Tahmasebpoor, S., Danielsson, A., Edlund, K., Asplund, A., Sjostedt, E.,
  Lundberg, E., Szigyarto, C.A., Skogs, M., Takanen, J.O., Berling, H., Tegel, H.,
  Mulder, J., Nilsson, P., Schwenk, J.M., Lindskog, C., Danielsson, F., Mardinoglu, A.,
  Sivertsson, A., von Feilitzen, K., Forsberg, M., Zwahlen, M., Olsson, I., Navani, S.,
  Huss, M., Nielsen, J., Ponten, F., Uhlen, M., 2014. Analysis of the human tissue-specific expression by genome-wide integration of transcriptomics and antibody-based proteomics. Mol. Cell Proteom. 13, 397–406.
- Johnson-Kerner, B.L., Roth, L., Greene, J.P., Wichterle, H., Sproule, D.M., 2014. Giant axonal neuropathy: An updated perspective on its pathology and pathogenesis. Muscle Nerve 50, 467–476.
- Johnson-Kerner, B.L., Garcia Diaz, A., Ekins, S., Wichterle, H., 2015. Kelch domain of gigaxonin interacts with intermediate filament proteins affected in giant axonal neuropathy. PLoS One 10, e0140157.
- Landrum, M.J., Lee, J.M., Benson, M., Brown, G.R., Chao, C., Chitipiralla, S., Gu, B., Hart, J., Hoffman, D., Jang, W., Karapetyan, K., Katz, K., Liu, C., Maddipatla, Z., Malheiro, A., McDaniel, K., Ovetsky, M., Riley, G., Zhou, G., Holmes, J.B., Kattman, B.L., Maglott, D.R., 2018. ClinVar: improving access to variant interpretations and supporting evidence. Nucleic Acids Res 46, D1062–D1067.
- Lescouzeres, L., Bomont, P., 2020. E3 Ubiquitin ligases in neurological diseases: focus on gigaxonin and autophagy. Front. Physiol. 11, 1022.

- Mahammad, S., Murthy, S.N., Didonna, A., Grin, B., Israeli, E., Perrot, R., Bomont, P., Julien, J.P., Kuczmarski, E., Opal, P., Goldman, R.D., 2013. Giant axonal neuropathy-associated gigaxonin mutations impair intermediate filament protein degradation. J. Clin. Invest. 123, 1964–1975.
- Renganathan, B., Zewe, J.P., Cheng, Y., Paumier, J.M., Kittisopikul, M., Ridge, K.M., Opal, P., Gelfand, V.I., 2023. Gigaxonin is required for intermediate filament transport. FASEB J. 37, e22886.
- Shao, C.Y., Zhu, J., Xie, Y.J., Wang, Z., Wang, Y.N., Wang, Y., Su, L.D., Zhou, L., Zhou, T. H., Shen, Y., 2013. Distinct functions of nuclear distribution proteins LIS1, Ndel1 and NudCL in regulating axonal mitochondrial transport. Traffic 14, 785–797.
- Sherman, B.T., Hao, M., Qiu, J., Jiao, X., Baseler, M.W., Lane, H.C., Imamichi, T., Chang, W., 2022. DAVID: a web server for functional enrichment analysis and functional annotation of gene lists (2021 update). Nucleic Acids Res. 50, W216–W221.
- Shi, X., Xiang, S., Cao, J., Zhu, H., Yang, B., He, Q., Ying, M., 2019. Kelch-like proteins: Physiological functions and relationships with diseases. Pharm. Res. 148, 104404

- Taipale, M., Tucker, G., Peng, J., Krykbaeva, I., Lin, Z.Y., Larsen, B., Choi, H., Berger, B., Gingras, A.C., Lindquist, S., 2014. A quantitative chaperone interaction network reveals the architecture of cellular protein homeostasis pathways. Cell 158, 434-448.
- Uchida, A., Alami, N.H., Brown, A., 2009. Tight functional coupling of kinesin-1A and dynein motors in the bidirectional transport of neurofilaments. Mol. Biol. Cell 20, 4997–5006.
- UniProt, C., 2023. UniProt: the universal protein knowledgebase in 2023. Nucleic Acids Res. 51, D523–D531.
- Vuolo, L., Stevenson, N.L., Heesom, K.J., Stephens, D.J., 2018. Dynein-2 intermediate chains play crucial but distinct roles in primary cilia formation and function. Elife 7.
- Zhou, T., Zimmerman, W., Liu, X., Erikson, R.L., 2006. A mammalian NudC-like protein essential for dynein stability and cell viability. Proc. Natl. Acad. Sci. USA 103, 9039–9044.